Color Imaging *via* Nearest Neighbor Hole Coupling in Plasmonic Color Filters Integrated onto a Complementary Metal-Oxide Semiconductor Image Sensor

Stanley P. Burgos,[†,§] **Sozo Yokogawa,**[†,‡,§] **and Harry A. Atwater**[†,*]

[†]California Institute of Technology, 1200 East California Boulevard, Pasadena, California 91125, United States, and [‡]Sony Corporation, Atsugi Tec. 4-14-1 Asahi-cho, Atsugi, Kanagawa 243-0014, Japan. [§]Equal author contribution.

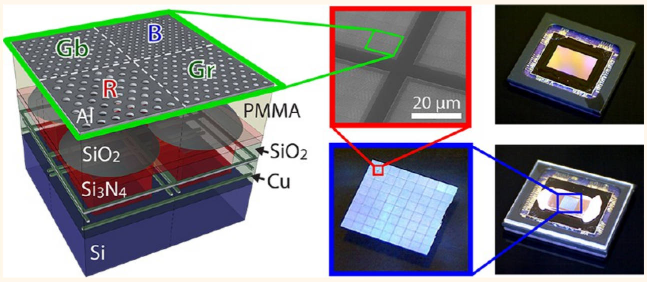

ABSTRACT State-of-the-art CMOS imagers are composed of very small pixels, so it is critical for plasmonic imaging to understand the optical response of finite-size hole arrays and their coupling efficiency to CMOS image sensor pixels. Here, we demonstrate that the transmission spectra of finite-size hole arrays can be accurately described by only accounting for up to the second nearest-neighbor scattering-absorption interactions of hole pairs, thus making hole arrays appealing for close-packed color filters for imaging applications. Using this model, we find that the peak transmission efficiency of a square-shaped hole array with a triangular lattice reaches $\sim$90% that of an infinite array at an extent of $\sim 6 \times 6\ \mu m^2$, the smallest size array showing near-infinite array transmission properties. Finally, we experimentally validate our findings by investigating the transmission and imaging characteristics of a 360 × 320 pixel plasmonic color filter array composed of $5.6 \times 5.6\ \mu m^2$ RGB color filters integrated onto a commercial black and white 1/2.8 in. CMOS image sensor, demonstrating full-color high resolution plasmonic imaging. Our results show good color fidelity with a 6-color-averaged color difference metric (ΔE) in the range of 16.6–19.3, after white balancing and color-matrix correcting raw images taken with f-numbers ranging from 1.8 to 16. The integrated peak filter transmission efficiencies are measured to be in the 50% range, with a FWHM of 200 nm for all three RGB filters, in good agreement with the spectral response of isolated unmounted color filters.

KEYWORDS: CMOS image sensor · hole array color filter

In contemporary Si-based image sensor technologies such as charge-couple devices (CCDs) and complementary metal-oxide semiconductor (CMOS) image sensors (IS), color sensitivity is added to photo detective pixels by equipping them with on-chip color filters, composed of organic dye-based absorption filters.[1] However, organic dye filters are not durable at high temperatures or under long exposure to ultraviolet (UV) radiation,[2] and cannot be made much thinner than a few hundred nanometers due to the low absorption coefficient of the dye material. Furthermore, on-chip color filter implementation using organic dye filters requires carefully aligned lithography steps for each type of color filter over the entire photodiode array, thus making their fabrication costly and highly impractical for multicolor and hyperspectral imaging devices composed of more than the three primary or complementary colors.

Meanwhile, it is well-known that plasmonic hole arrays in thin metal films can be engineered as optical band-pass filters owing to the interference of surface plasmons (SPs) between adjacent holes.[3−5] Unlike current on-chip organic color filters, plasmonic filters have the advantage of being highly tunable across the visible spectrum and requiring only a single perforated metallic layer to fabricate many colors.[6−8] Plasmonic hole array color filters have recently been integrated with a CMOS image sensor, demonstrating filter viability in the visible;[9,10] however, full-color imaging using the

* Address correspondence to haa@caltech.edu.

Received for review July 31, 2013 and accepted October 24, 2013.

Published online October 24, 2013
10.1021/nn403991d

© 2013 American Chemical Society

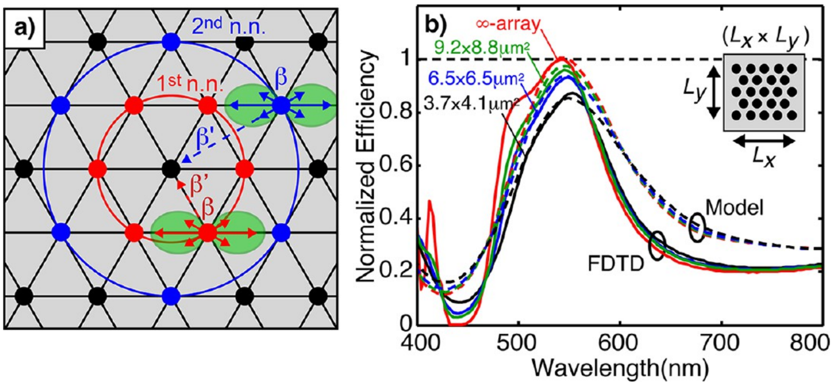

Figure 1. Schematic of the second nearest-neighbor (n.n.) scattering-absorption model used to reconstruct the transmission spectra of a square-shaped triangular-lattice hole array. The black circles in (a) represent holes in a triangular lattice, connected by black lines for reference. The first and second nearest neighbors surrounding the central lattice site are shown in red and blue, respectively. The scattering intensity of a contributing lattice site is depicted by green ovals, with the enclosed arrows corresponding to the spatial scattering efficiency amplitudes (β). The absorption efficiencies (β') of the central lattice site are depicted by dashed arrows. (b) Transmission efficiency curves extracted from the nearest-neighbor model (dashed curves) and FDTD (solid curves) as a function of array size for the square-shaped triangular-lattice hole array shown on the inset, consisting of 180 nm diameter holes set at a pitch of 340 nm in a 150 nm thick Al film embedded in SiO_2. The dashed red curve corresponds to a 40 × 40 μm^2 array for the model, which we call '∞-array' due to its asymptotic behavior compared to FDTD (red, solid curve). We normalize each set of data to these infinite-array curves for reference. The other curves correspond to normalized transmission efficiencies for different size hole arrays, ranging from ~4 × 4 to 10 × 10 μm^2 in size.

plasmonic color filter technology platform has, to date (2013), not been reported. In recent studies, several filter performance aspects necessary for state-of-the-art image sensor application have been reported, such as filter transmission dependence on array size, spatial color-crosstalk, and robustness against defects.[8,11−13]

RESULTS AND DISCUSSION

Nearest-Neighbor Scattering-Absorption Hole Array Model. Here, by investigating the scattering-absorption efficiencies of surface plasmons between hole pairs in a hole array, we demonstrate that we can reconstruct the transmission spectra of large-size hole arrays by only accounting for up to second nearest-neighbor interactions within the array. The scattering-absorption efficiencies are found by fitting finite-difference time-domain (FDTD) transmission data to a scattering-absorption model consisting of a truncated Fabry−Pérot resonance between hole pairs (see Methods).[14,15] Although subwavelength holes are known to scatter both circularly expanding SPs[14−16] as well as 'regular' linear SPs,[17] in this model we only account for the scattering contribution of circular SPs, which we find dominate the transmission spectra of the array. The scattering-absorption coefficients, extracted from FDTD simulations for a symmetric 4-hole triangular-lattice unit cell (Figure S1a), are shown in Figure S1c. The unit cell used for the fit consists of 180 nm diameters holes in a 150 nm thick Al film embedded in SiO_2.

By spectrally resolving this scattering-absorbing coefficient, we find that it has a maximum amplitude at a surface plasmon wavelength that is roughly twice the diameter of the hole (see Figure S1c), *i.e.*, $d \sim \lambda_{SP}/2$.[18,19] Since the transmission of the array is expected to be dominated by the amplitude of the scattering-absorption efficiency coefficient, in selecting the hole diameter best suited for filtering a given color, we need only to look for the maximum of this curve. Thus, in looking at Figure S1c, we see that a 180 nm hole is best suited for filtering ~550 nm (green) wavelength light. By following a similar fitting process for different size holes, we find that the best-suited holes for filtering red (~650 nm) and blue (~450 nm) wavelengths are $d = 240$ nm and $d = 140$ nm, respectively, in agreement with known values found experimentally.[12]

Given these combined scattering-absorption efficiencies, in order to build a nearest neighbor model, we need to determine how these efficiencies contribute to the transmission spectra of finite-size hole arrays. Since we are treating the transmission of a hole array as a superposition of scattering-absorption events between hole pairs, in considering the contributing scattering events surrounding a given hole site, it is sensible to only consider those scattering events that occur at hole positions that are in the 'line-of-sight' of the hole of interest. Thus, to first order, we approximate the transmission of an array by only considering up to second nearest-neighbor interactions, since scattering from holes at larger distances can be thought of as being 'screened' by the first and second nearest-neighbors (see Figure 1a). To validate the accuracy of the second nearest-neighbor scattering model, we compare the transmission spectra of several large-size hole array configurations obtained by both FDTD (Figure 1b, solid curves) and the model (Figure 1b, dashed curves), with both spectra in good agreement of each other. We note that the second-nearest-neighbor approximation is only valid for hole arrays in which the array extent is much larger than the second nearest neighbor distance, with smaller arrays requiring third and higher-order nearest neighbor contributions to properly set the in-plane phase that determines their transmission spectra (see Figure S2).

Hole Array Filter Design. Considering a ~10 × 10 μm^2 hole array configuration composed 180 nm diameter holes in a triangular lattice, we note that the position of the transmission peak can be tuned by varying the period (or lattice constant) of the array (see Figure S3a). However, the amplitude of the transmission peak is maximum for periodicities where the transmission peak has greatest overlap with the amplitude of the SP scattering-absorption coefficient (see Figures S1c and S3a). Thus, we find that the optimal pitch for filtering ~550 nm (green) wavelength light with 180-nm-diameter holes is $p \sim 340$ nm. By following a similar period variation for the 240 and 140 nm diameter holes, we find that their optimal pitch for filtering red (~650 nm) and blue (~450 nm) wavelength light are 420 and 260 nm, respectively. These (p,d) values for filtering RGB color light were verified with FDTD simulations by doing small variations around the predicted values.

Having found the optimal (p,d) values for filtering RGB light, we use the model to determine the transmission properties of finite-size hole arrays as they pertain to imaging applications. More specifically, we are looking for the smallest-size hole arrays showing near-infinite transmission properties. To do this, we calculate the transmission spectra of a square-shaped triangular-lattice array as a function of hole array size (Figure 1b). Starting with a ~3 × 3 μm^2 hole array, which is comparable to the size of a CMOS IS pixel, we systematically add rows and columns to the array and monitor the evolution of the transmission efficiency spectra, normalizing to an infinite array for reference. In evaluating the asymptotic behavior of the spectra, we find that the finite-size array spectra is already at ~80% the peak efficiency of an infinite array for sizes as small as ~4 × 4 μm^2, consisting of only 10 × 12 = 120 holes, ~1/3 the amount required for a square lattice array,[20] we suspect due to the difference in hole filling fraction, which should influence the scattering-absorption interactions of hole pairs.

Continuing in this manner, the peak transmission value increases to ~90% for ~6 × 6 μm^2 array sizes, with only a minimal increase beyond ~10 × 10 μm^2. Thus, we find that ~6 × 6 μm^2 is the smallest-size array showing near-infinite array transmission properties, with any additional increase in size only bringing marginal benefit to the transmission efficiency. To demonstrate this, we fabricate and integrate a 360 × 320 pixel plasmonic color filter array composed on 5.6 × 5.6 μm^2 RGB color filters integrated onto a commercial black and white 1/2.8 in. CMOS image sensor and analyze the transmission and image quality of high-resolution color images taken with the integrated plasmonic device.

Fabrication and Integration. For the color filter array layout, we used the Bayer pattern, which consists of a 2 × 2 color unit cell with two green filters (Gb, Gr) in the diagonal positions (the lower case letter following the G corresponds to the color that is horizontally next to the green filter), and blue (B) and red (R) in the off-diagonal positions (Figure 2b). Each individual hole array color filter was designed with the size of 5.6 × 5.6 μm^2, which was exactly twice the pixel size of the CMOS image sensor in order to account for alignment errors in the integration (see Methods and Figure S5). Electron-beam lithography and lift-off were used to stitch 180 × 160 Bayer unit cells onto a quartz substrate (see Methods and Figure S4), resulting in a 360 × 320 pixel plasmonic color filter array with the dimensions of 2016 × 1792 μm^2 (Figure 2c,d). Here, we see 11.2 μm wide grid lines separating 40 × 40 filter blocks (corresponding to 224 × 224 μm^2), which were created during the fabrication process to both prevent overexposure of the peripheral region of each block during electron-beam lithography and to serve as guide lines for alignment with the CMOS image sensor pixel array.

For the integration, we used a front-side-illumination black and white CMOS image sensor composed of 1920 × 1200, 2.8 × 2.8 μm^2 pixels, corresponding to an effective pixel area of 5376 × 3360 μm^2 (Figure 2f). The integration was done by directly contacting the color filter array onto the CMOS image sensor (see Methods and Figure S4). As shown in Figure 2e, due to the difference in size between the plasmonic color filter array and the CMOS IS chip, only the center 1/3 of the horizontal area and 3/5 of the vertical area of the CMOS image sensor was equipped with plasmonic color filtering functionality.

Coupling Efficiency. The optical efficiency of the color filter design was assessed with spectral transmission measurements of isolated 22.4 × 22.4 μm^2 size RGB plasmonic hole array filters (see Methods). The resulting spectra, plotted in Figure 3a, show all three RGB filter designs having peak efficiencies in the 50–60% range with FWHM in the 150–200 nm range, consistent with the transmission data extracted from full-field electromagnetic simulations of unmounted plasmonic color filters embedded in a quartz matrix illuminated at normal incidence (Figure 3c). We note that due to the relatively large size of the hole array color filters (5.6 × 5.6 μm^2) and the fact that there was *no* separation between different color patches, we did not observe any significant interpatch resonances in the transmission spectra of each color filter, as is the case for smaller hole arrays with comparable interpatch separation distances,[21] thus allowing us to model the RGB color filters as infinite arrays for computational efficiency (see Figure S6a).

With these spectra as a benchmark for the color filter design, the transmission efficiencies of the plasmonic RGB filters as integrated onto the CMOS image sensor were estimated by comparing the output signal

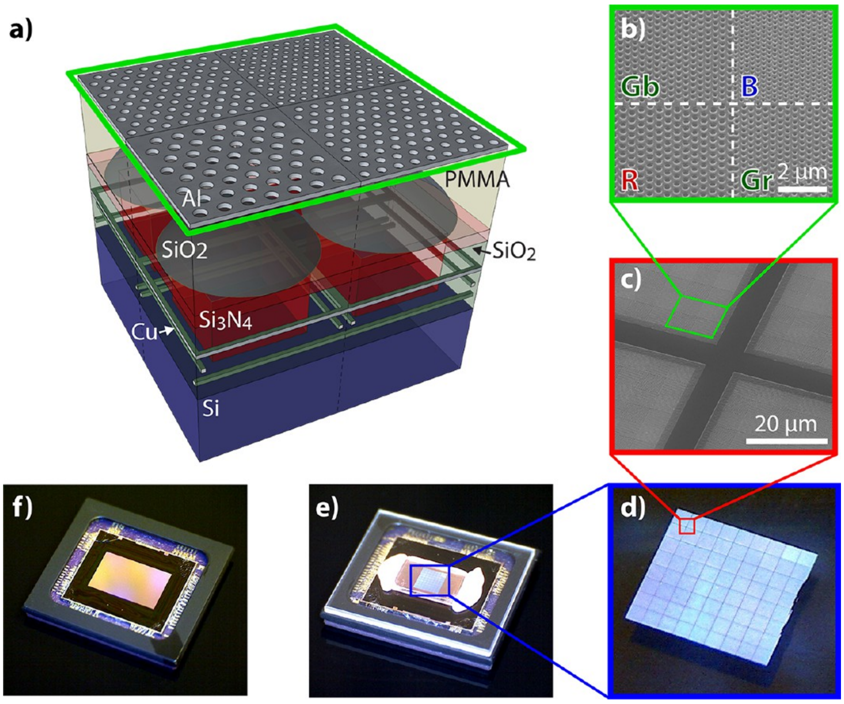

Figure 2. Hole array filter integrated with CMOS image sensor. (a) Schematic of front-side-illumination CMOS image sensor integrated with RGB plasmonic hole array filters in Bayer mosaic layout. (b) Scanning electron micrograph of RGB hole array filters in Bayer layout. (c) Scanning electron micrograph of 11.2 μm alignment grid lines separating 40 × 40 filter blocks. (d) Image of full 360 × 320 pixel (2016 × 1792 μm^2) plasmonic hole array filter pattern on quartz. Each square on the image corresponds to a 40 × 40 filter block (224 × 224 μm^2) separated by 11.2 μm alignment grid lines. (e) Image of CMOS image sensor integrated with the plasmonic hole array color filter. The white on the far edges of the integrated device corresponds to electronic grade putty used to hold the filter in place after alignment. (f) Image of CMOS image sensor before integration.

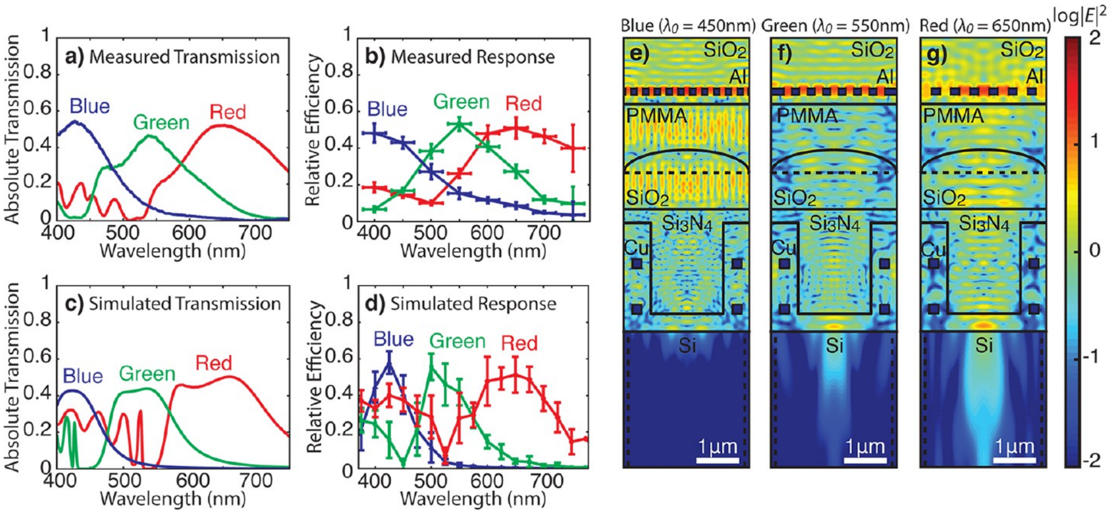

Figure 3. Integrated CMOS image sensor response. (a) Measured and (c) simulated spectral response of unmounted RGB plasmonic hole array filters. (b) Measured and (d) simulated relative efficiency of the CMOS image sensor integrated with the RGB hole array color filters. The horizontal error bars correspond to the spectral width of the band-bass filter used for the measurements and the vertical error bars correspond to averaged data. Simulation field map cross-sections taken at the center of the pixel and at the center transmission wavelengths for the (e) blue (λ_0 = 450 nm), (f) green (λ_0 = 550 nm), and (g) red (λ_0 = 650 nm) hole array color filters integrated with the CMOS image sensor.

of the pixels with color filters (corresponding to either R, G, or B) and those without (corresponding to white light). The color bands of interest were selected using narrowband band-pass filters with a FWHM of 40 nm and center wavelengths ranging from 400−750 nm in 50 nm steps. For each filter, and under constant lighting conditions, an image was taken of a uniform-color gray wall using a C-mount lens with a focal length of 12.5 mm and an f-number of 5.6. The resulting data is plotted in Figure 3b.

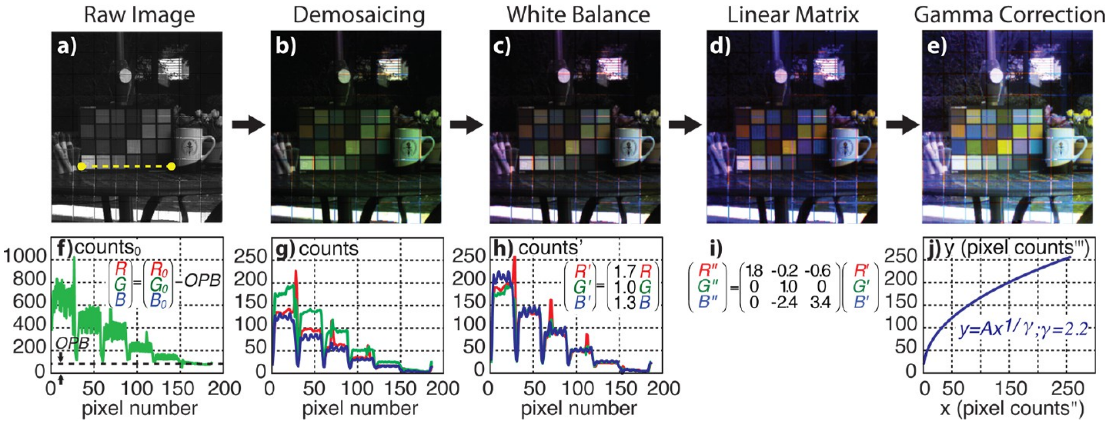

Figure 4. Image reconstruction process. (a) Raw 10-bit data (0−1023) image of a 24-patch Macbeth color chart positioned in a scene taken with the hole array filter integrated with the CMOS IS camera. The image was then converted to 8-bit data (0−255) for further signal processing, which came in the form of (b) demosaicing, (c) white balancing, (d) linear matrix correction, and (e) gamma correction. The yellow dashed line in (a) shows the position where the pixel signal is measured (in counts) in (f−h), corresponding to the images above them. (i) Linear matrix used on image after applying white balance to remove color cross talk. (j) Gamma transformation used to convert the image sensor's linear response to brightness to the logarithmic response of the human eye.

Direct comparison of the transmission efficiencies between the unmounted (Figure 3a) and CMOS integrated (Figure 3b) plasmonic color filters gives a quantitative measurement of how well the plasmonic color filters were integrated onto the CMOS image sensor. In comparing these two data sets, we see that the integrated-device peak transmission efficiencies are in the 50% range, which is only slightly lower than those of the unmounted color filters; indicating that although the direct contact integration scheme was not optimal, it did not significantly degrade the coupling efficiency. More specifically, because the color filter was integrated by simply pressing the RGB hole array color filters into intimate contact with the image sensor, we expected that there could be a low refractive-index gap between the bottom of the plasmonic filters and the top surface of the image sensor that could reduce the light coupling efficiency. However, we find from full-field electromagnetic simulations of the integrated device that the experimentally measured light coupling efficiencies shown in Figure 3b are in the same range as those simulated under perfect light coupling conditions, *i.e.*, in intimate mechanical contact (Figure 3d), indicating that the integration was nearly ideal.

The resulting simulated steady-state intensity field distributions of the three integrated color filters at their center wavelengths are shown in Figures 3e−g, showing that a significant factor in the high light-coupling efficiency in going from the hole array filter to the active Si area of the CMOS IS comes from the intermediate photonic nitride waveguide which directs the filtered light transmitted through the hole array filters into the active region of the Si image sensor pixel. We also note that, as expected, the simulations indicate that blue light absorption occurs in the Si pixel near the top surface region, while green light absorption occurs at a depth of approximately 1 μm, and red light absorption occurs at a depth of approximately 3 μm below the Si surface.

Because of computation restrictions, these simulations were done for device arrays of the *same* color (see Methods), so in order to investigate the effect of spatial color crosstalk in the integrated device, we modeled the 11.2 × 11.2 μm^2 Bayer unit cell by itself (without the device layer), and monitored the transmission right underneath the Bayer unit cell ($z = 0$ μm) and at $z = -1$ μm, where the focusing microlenses are located in the device simulations. The resulting spectra are shown in Figure S6b, from which we can see that, at least for the case of normal incidence, there is very little color crosstalk between different color hole array filters in the array, indicating that there should also be negligible crosstalk in the integrated plasmonic filter in the form of different color light scattering into adjacent pixels after light is coupled through the plasmonic filters into the focusing microlenses.

Plasmonic Imaging. Having verified the plasmonic color filter transmission efficiency as integrated onto the CMOS image sensor, we demonstrate full-color, high resolution camera performance by taking full color images using a 12.5 mm lens and a 5.6 f-number, corresponding to a half-aperture angle of 5°. Under these conditions, in Figure 4a, we display a representative raw image taken of a 24-patch Macbeth color chart positioned in a scene. In Figure 4f, we plot the signal of the pixels indicated by the dashed yellow line in Figure 4a, which span across the gray color patches on the Macbeth color chart. At this point, each pixel has 10-bit data, ranging from 0 to 1023, and we subtract the optical black (OPB) signal from the image, which corresponds to a dark current signal offset, as indicated in Figure 4f. The image is then converged to 8-bit data, ranging from 0 to 255, for further signal processing.

However, since the active pixels on the CMOS image sensor are filtered by a Bayer color filter array, each pixel only has *intensity* information of one of the three primary colors. To reconstruct the full-color image, a bilinear demosaicing algorithm is used to interpolate the set RGB values for each pixel from its neighbors. For example, the red value of a nonred pixel is computed as the average of the two or four adjacent red pixels, and similarly for blue and green. The resulting bitmap image after demosaicing is shown in Figure 4b, with corresponding RGB signal levels (ranging from 0−255 due to 8-bit conversion) shown in Figure 4g.

After demosaicing, the image is white balanced by equalizing the RGB signal levels of the gray patches on the Macbeth color chart (Figures 4c,h). Next, we apply a linear matrix correction to correct for the filters' spectral color crosstalk (Figures 4d,i). Here, we see that the red pixels are applied a transformation that subtracts green and blue values from it, $R'' = 1.8R' - 0.2G' - 0.6B'$, as expected since the red pixels experience the most color crosstalk as seen from the spectra plotted in Figure 3. Similarly, the blue pixels are subtracted a nearly equal amount of the green spectra from itself, $B'' = -2.4G' + 3.4B'$, in order to shift the original blue filters' spectral response further into the blue. However, we leave the green filter spectra untouched, $G'' = 1.0G'$, since subtracting any amount of red or blue from the green would significantly reduce its counts due to their large spectral overlaps (see Figure 3). To realize a purer green spectra with a much narrower FWHM and smaller linear matrix cross-terms, we would need to incorporate slightly smaller filter hole diameters, or apply novel filtering structures having higher transmission efficiency with narrower FWHM than those of hole array filters.[22] However, we note that for the case of reducing the hole diameter, it would need to be accompanied with a change in pitch (to compensate for the effective surface plasmon path length between holes), ultimately having the overall effect of reducing the array transmission efficiency (Figure S3b).

After applying the linear matrix pixel transformation, a gamma correction (Figure 4j) is applied to convert the image sensor's linear response to brightness into the logarithmic response of the human eye. The result is the natural-color image shown in Figure 4e. Here we see the 11.2 μm alignment grid lines, which contain 40 color pixels in between them, along the two normal directions.

Color Quality Evaluation. The color quality of the image can be measured using the CIE ΔE 2000 metric,[23] which measures the color difference between the reference color on a Macbeth color chart and what the color actually is in the signal-processed image (Figure 4e). *Via* this metric, the higher the ΔE, the more noticeable the color difference is to the human eye, with $\Delta E = 1$ being regarded as a 'just noticeable' difference. Using established color code standards,[23] the measured CIE ΔE of the integrated CMOS image sensor increases from 3.8 for blue, to 10.2 for green, and 28.6 for red, reflecting the fact that the hole array filter design is efficient at filtering short (blue) wavelengths but has increasing spectral color crosstalk from the shorter wavelengths as the hole array pitch and diameter is increased to filter the longer green and red wavelengths.[12] Note that the ΔE (color difference) being measured here is after signal processing, meaning that the filters' original spectral response (see, *e.g.*, Figure 3b,d) have already been modified, in particular with the linear matrix correction (see Figure 4d,i), which corrects for the filters' original spectral color crosstalk.

Similarly, for the complementary colors, which can be considered as linear superpositions of the primary colors, the measured ΔE is 5.7 for yellow (green + red), 24.7 for magenta (red + blue), and 33.3 for cyan (blue + green), which is consistent with the ΔEs of the primary colors that compose them. Averaging the ΔE values of the three primary and three complementary colors, we get an averaged ΔE of 17.7 for the integrated CMOS image sensor, a value which, although not ideal, is capable of capturing vivid full-color images, as demonstrated in Figure 4e. Following this image reconstruction process, we show in Figure S7 several additional images taken with the integrated CMOS image sensor, other demonstrations of the technology's versatility with respect to focal length and outdoor lighting conditions.

As a visual reference of how these ΔE values for the integrated plasmonic CMOS IS device translate to actual differences in color space, we plot in Figure 5a a graphical representation of the extracted RGB and CYM ΔE values on a different metric called the CIE $L^*a^*b^*$ chromaticity diagram, together with the corresponding color limits proposed by Matsushima *et al.* as the current (2013) color standard for the image sensor community.[24] In this metric, we integrate over the L^* variable (which measures the lightness of a color), allowing us to plot the color value on the a^*b^* color-space plane, where a^* roughly ranges from green to magenta and b^* from blue to yellow in going from negative to positive values, respectively. The colors measured from the image taken with the 5.6 f-number plasmonic camera are represented on this diagram by small green filled dots encircled by an oval labeled by the color they represent. As can be seen from this image, consistent with the ΔE values discussed above, blue and yellow come the closest to the color standard, with green and cyan being the next closest, and red and magenta coming in furthest from their respective color standards. As a reference of how these a^*b^* distances (or corresponding ΔE values) correspond to actual colors on an image, we include in Figure 5 images of a 24-patch Macbeth color chart taken with the plasmonic CMOS IS camera (Figure 5b) and a conventional CMOS IS camera (Figure 5c), with both

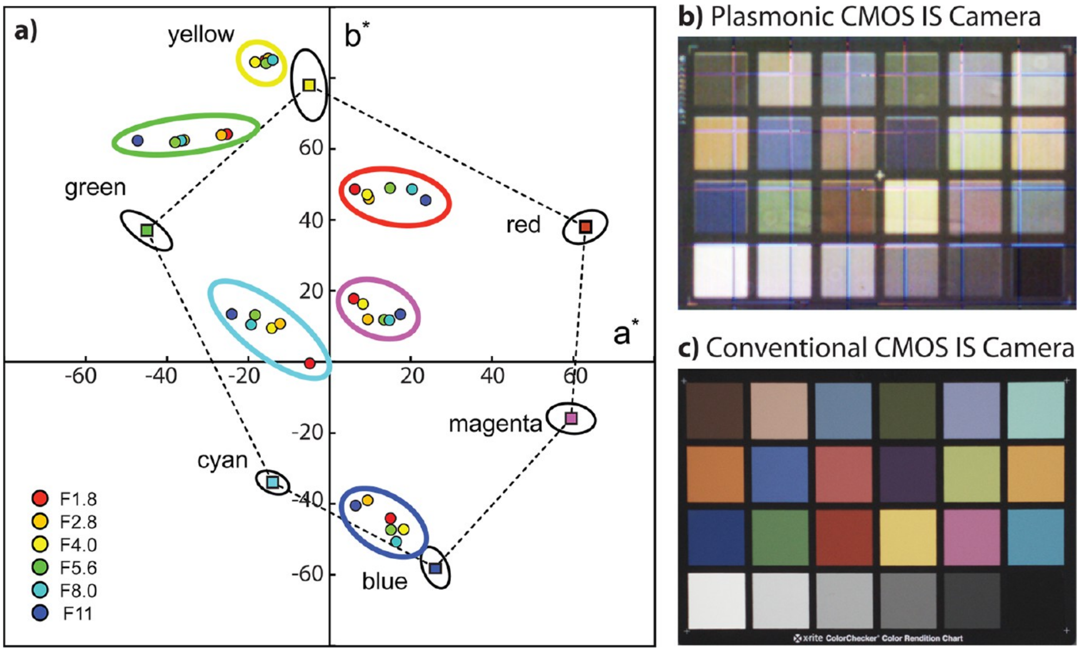

Figure 5. Color performance of hole array color filter integrated with CMOS IS. (a) CIE L*a*b* chromaticity diagram containing the converted tabulated ΔE values from Table 1 for the performance of the integrated hole array color filter CMOS IS as a function of f-number (acceptance angle). The different f-numbers (columns of Table 1) are color coded on the chromaticity diagram by small filled colored dots and the colors being measured (rows of Table 1) are both labeled by the color name and circled by an oval of the corresponding color. The RGB and CMY colors as defined by Matsushima *et al.* as the current (2013) color standard for the image sensor community[24] are shown by colored squares encased by an oval that corresponds to the allowed limits proposed for that color. Images of a 24-patch Macbeth color chart taken with the plasmonic CMOS IS camera (b) and a conventional CMOS IS camera (c), with both images undergoing similar signal processing as described in Figure 4.

images undergoing similar signal processing as described in Figure 4.

F-Number Dependence. These representative images were taken with a 5.6 f-number, corresponding to a nearly normal incident half-aperture angle of 5°; however, for proper filter performance, it is important to check that the RGB hole array filters retain their designed filtering functionality for larger aperture angles. To investigate this, we simulated the transmission of unmounted plasmonic color filter arrays for incidence angles ranging from 0 to 30°. The resulting spectra for the green color filter is plotted in Figures 6a,b. As can be seen from these figures, the filter does have an angular dependence;[25,26] however, in order to see if this spectral variation will play a significant role in the filter functionality, we need to consider what range of incidence angles we are collecting for a given f-number (*F*). From the definition of f-number, which is the ratio of focal length (*f*) to aperture diameter (*D*), the half-aperture angle for a given f-number is equal to $\theta_{1/2} = \arctan(1/2F)$. This means that for an f-number of 16, the maximum half-aperture collection angle will be 1.8°, meaning that the image sensor will be collecting nearly collimated incident light. As a result, the filtering functionality should be consistent with the normal-incidence filter designs for images taken with large f-numbers.

However, for an f-number of 1.8, the half-aperture angle is 15.5°, which referring to Figures 6a,b, should have some effect on the quality of the image color. The extent to which the image will be affected by off-normal incident light is determined by the pixel signal, integrated over the range of incidence angles accepted by its f-number. Thus, in considering the transmission through a given filter color, operating with a given f-number, we need to average over incidence angle (within its aperture angle) and polarization (to account for unpolarized light). For example, for the green filter operating with an f-number of 1.8, we estimate the integrated-device's spectral response by averaging the filter angular transmission response for incident angles within its 15° acceptance angle and over both TE and TM polarizations. The resulting averaged spectrum is plotted in Figure 6c, from which we can see that it is similar to the normal incidence spectrum. Thus, we should expect to see admissible difference in the color of images taken with large f-numbers (corresponding to small acceptance angles) and small f-numbers (corresponding to large acceptance angles).

To confirm the f-number dependence, we took several images of a 24-patch Macbeth color chart using a 50 mm lens and changing the f-number from 1.8 to 16 (see Figures 6d–i). As expected, the colors look visibly constant among all the f-number images, showing slightly dimmer color for smaller f-numbers due to the larger acceptance angles. The color is again analyzed using the standard color error index, CIE ΔE 2000,[23] which when averaged over the three primary

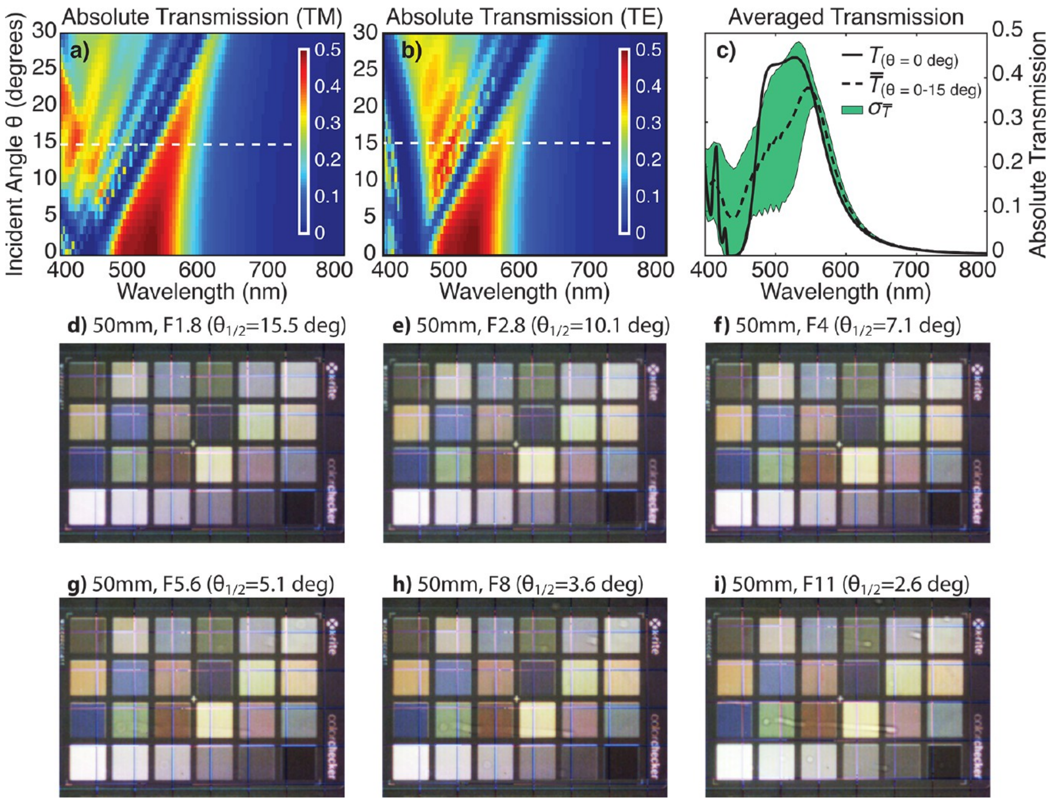

Figure 6. Green filter angular response and integrated CMOS IS f-number dependence. Simulated spectral transmission response of green hole array filter as a function of incident angle for (a) TM and (b) TE polarizations. (c) Simulated spectral response of green filter operating with a maximum half-aperture angle of 15°, corresponding to an f-number of about 1.8, obtained by averaging the spectral response for incident angles ranging from 0 to 15° over both polarizations. Images of 24-patch Macbeth color chart taken with the CMOS image sensor integrated with the RGB plasmonic hole array filter with a 50mm lens and an f-number (maximum half-aperture angle) of (d) 1.8 (15.5°), (e) 2.8 (10.1°), (f) 4 (7.1°), (g) 5.6 (5.1°), (h) 8 (3.6°), and (i) 11 (2.6°).

TABLE 1. F-Numbers and Their Respective Standard Color Error Index (CIE Δ*E* 2000)

F-number	1.8	2.8	4.0	5.6	8.0	11	16
$\theta_{1/2}$ (deg)	15.5	10.1	7.1	5.1	3.6	2.6	1.8
Blue	4.0	5.8	2.9	3.8	3.7	7.0	3.7
Green	15.1	14.5	11.0	10.2	10.7	8.3	10.1
Red	34.4	31.3	32.1	28.6	25.0	21.6	27.5
Yellow	5.9	5.5	7.0	5.7	5.1	5.6	5.8
Magenta	34.6	27.5	31.7	24.7	23.9	23.7	24.6
Cyan	20.7	31.3	30.1	33.3	31.3	33.6	32.6
6 color average	19.1	19.3	19.1	17.7	16.6	16.6	17.4

(red, green, blue) and three complementary (yellow, magenta, cyan) colors, shows a small variation of only 2.8 in going from an f-number of 16 to 1.8 (see Table 1). For the primary colors, note that the CIE Δ*E* 2000 values for blue are smaller than those of green and red across all f-numbers, demonstrating that, independent of incident angle, the plasmonic color filter design retains its good color fidelity for shorter wavelengths owing to the suppression of the photonic modes, which remain accessible for the longer-wavelength hole array filter diameters.[12] Further improvement of the color fidelity between red and blue filters is an important research direction for the development of plasmonic imaging technology.[22,27−29]

For visual reference, the f-number dependent RGB and CYM CIE Δ*E* values are plotted on the CIE L*a*b* chromaticity diagram (Figure 5a), as before, together with the corresponding color limits proposed by Matsushima *et al.* as the current (2013) color standard for the image sensor community.[24] The different f-numbers (columns of Table 1) are color coded on the chromaticity diagram by the small filled colored dots and the colors being measured (rows of Table 1) are both labeled by the color name and circled by an oval of the corresponding color. As can be seen from this image, consistent with the small variance observed in the Δ*E* measurements, all the colors are grouped around the same area in color-space as a function of f-number, demonstrating the technology's versatility with respect to acceptance angle.

CONCLUSION

In this article, through the use of a comprehensive scattering model for describing the transmission spectra of finite-size hole array filters, we have designed and demonstrated the imaging characteristics of a CMOS image sensor integrated with a primary color

(RGB) plasmonic filter that is competitive with conventional dye-filter technology in terms of transmission and insensitivity to f-number (incident angle), all with a single lithographic step. The ability to add color sensitivity to an image with a single perforated metallic layer, with its corresponding spectra determined by nearest-neighbor interactions, not only reduces the complexity and cost of fabricating tricolor filters, but also allows for new technology such as hyperspectral imaging devices for sensing that consist of any number of colors. In this work, the integration was done by directly contacting the plasmonic color filter array onto the CMOS image sensor, which already showed almost optimal integrated transmission efficiencies; however, future filter-chip integration will require the fabrication of the plasmonic color filter directly onto the CMOS image sensor. Although the hole array filter dimensions are subwavelength, with the smallest interhole spacing being only 120 nm for the blue color filter, these dimensions are compatible with conventional deep-ultraviolet photolithography, an attractive feature for large-scale manufacturing.

METHODS

Scattering-Absorption Model. Using FDTD, we simulated the transmission spectra of a symmetric triangular lattice unit-cell consisting of a 4-hole diamond-shaped configuration (Figure S1a) as a function of pitch and wavelength. The holes are modeled as 180 nm diameter SiO_2 cylinders in a 150 nm Al film cladded from top to bottom by SiO_2. Since the scattering-absorption efficiencies are expected to be wavelength dependent, we fit the spectra by fixing the wavelength and fitting the hole-pair scattering-absorption model as a function of pitch.[14] The FDTD data along with the fitted curve are shown in Figure S1b for $\lambda_0 = 400$ nm, from which we can see excellent agreement between the simulation and model results. By varying the wavelength and repeating the fitting procedure, we extract the spectrally resolved complex-valued scattering-absorption parameters for a given diameter hole (see Figure S1c).

Fabrication and Integration. Fabrication of plasmonic hole array filter was done using electron-beam lithography and lift-off (see Figure S4). A thin Cr layer was used to reduce charging of the quartz substrate during patterning (Figure S4a) and a 150 nm Al layer was used for the final hole-array filter metal layer (Figure S4e). After developing, a 300 nm thick layer of spin-on-glass (SOG) was used to infill the hole array filters (Figure S4g). Once fabricated, the integration was done by directly contacting the color filter array onto the CMOS image sensor (Figure S4k), using PMMA to first planarize the microlenses of the image sensor (Figure S4j).

Alignment. Alignment of the hole array filter with the CMOS image sensor was done by hand using a microscope. Since each individual color in the 360 × 320 RGB filter array was designed to be exactly twice the pixel size of the CMOS image sensor (see Figure S5a), small translational misalignments were easily corrected by selecting either the even or odd pixels in each direction of the CMOS image sensor array (see Figure S5b). Note that rotational misalignments (Figure S5c) cannot be corrected using this scheme since the rotational alignment error is not constant throughout the chip. After aligning the filter array as best as possible, we used electronic grade putty to hold the filter in place.

Alignment Check. To check the alignment, an image was taken of a gray wall, and the color uniformity was checked for the different parity set of pixels after demosaicing the image but before applying white balance, *i.e.*, before equalizing the RGB value readouts. Thus, the gray color of the wall appears green since the green pixels have a larger signal than the red and blue pixels before they are equalized by the white balance transformation ($R,G,B = 1.7,1.0,1.3$). The images for the different parity set of pixels are shown in Figure S5d, with the even−even (EE), even−odd (EO), odd−even (OE), and odd−odd (OO) pixel readouts showing a spatial color map which varies from green to magenta. The green areas correspond to pixels that are entirely covered by a single color filter in the RGB filter array (see, *e.g.*, Figure S5b), and the magenta areas correspond to pixels that are sitting predominantly at the boundaries between different color filters (see, *e.g.*, Figure S5c).

Transmission Measurements. Spectral transmission measurements of isolated unmounted 22.4 × 22.4 μm^2 RGB plasmonic hole array filters were performed on an inverted microscope coupled to a grating spectrometer and liquid nitrogen cooled CCD system. The sample was illuminated with a collimated halogen lamp filtered by a temperature conversion filter that gave a sun-like blackbody emission (color temperature of 5500 K). All filter spectra were measured with a spectrometer utilizing a 100 × 1340 pixel liquid nitrogen cooled CCD detector with sensitivity in the 300−800 nm wavelength range. The transmission spectrum of each hole array filter was divided by the spectrum of an open window of the same size in order to measure the absolute transmission of each filter.

Transmission Simulations. The transmission of isolated RGB filters was simulated using the FDTD algorithm (Lumerical Solutions 7.0) with a single unit cell of the hexagonal Al hole-array lattice embedded in quartz with Bloch boundary conditions in the in-plane directions and perfectly matched layer (PML) boundary conditions in the excitation direction. The spatial mesh size was varied from 2 to 8 nm, with little spectral difference observed within that range; however, since these simulations are computationally small due to the Bloch boundary conditions used, we used the smallest mesh size of 2 nm for maximum accuracy. Complex optical constants for Al and SiO_2 were taken from tabulated data.[30] For normal incidence simulations, the structure was excited with a broadband planewave source and the steady-state electromagnetic fields were recorded on the opposite side of the structure. The transmission of the structure was calculated as the time-average of the Poynting vector normalized by the source. For angled illumination, it was done similar to the normal incidence simulations, except that care was given to the angles imposed by the Bloch boundary condition on all the wavelengths.

Integrated Simulations. The steady-state field response of the integrated structure (Figure 1a) was simulated using the FDTD algorithm. Similar to the transmission simulations, a 2 nm mesh was also used for these simulations; however, as mentioned in the text, due to computations restrictions, these simulations were done with *periodic* boundary conditions, meaning that we simulated a device in which the *same* color pixel repeated in the direction transverse to the device axis. We note that another set of transmission simulations was performed on just the RGB hole array Bayer unit cell to determine the existence of any sort of spatial crosstalk in the form of different color light scattering into adjacent pixels after light is coupled through the plasmonic filters into the focusing microlenses (see main text for details). Complex optical constants for Al, SiO_2, Si_3N_4, and Si were taken from tabulated data;[30] PMMA was modeled as SiO_2, and Cu as a perfect electric conductor (PEC) in order to reduce the simulation time. The structure was illuminated with a broadband planewave and the steady-state electromagnetic fields were recorded at the center cross section of the structure (Figures 3e−g) to observe the field distribution response.

Conflict of Interest: The authors declare no competing financial interest.

Supporting Information Available: Details about the nearest-neighbor scattering-absorption model and its dependence on configuration size and number of included nearest neighbors; pitch and diameter dependence of infinite hole arrays investigated both with FDTD and the nearest-neighbor model; details of fabrication process flow as well as alignment procedure;

RGB Bayer unit cell filter transmission compared to that of infinite RGB arrays as well as details of crosstalk analysis in Bayer unit cell; and versatility of integrated hole array CMOS IS as a function of focal length and outside lighting conditions. This material is available free of charge *via* the Internet at http://pubs.acs.org.

Acknowledgment. The authors gratefully acknowledge critical support and infrastructure provided by the Kavli Nanoscience Institute at Caltech. S. Burgos appreciatively acknowledges support from the National Science Foundation Graduate Fellowship. This work was supported by the Air Force Office of Scientific Research under a Multidisciplinary University Research Initiative grant FA9550-10-1-0264 and under grant FA9550-09-1-0673.

REFERENCES AND NOTES

1. Nakamura, J. *Image Sensors and Signal Processing for Digital Still Camera*; CRC Press: Boca Raton, FL, 2006.
2. Inaba, Y.; Kasano, M.; Tanaka, K.; Yamaguchi, T. Degradation-Free MOS Image Sensor with Photonic Crystal Color Filter. *IEEE Electron Device Lett.* **2006**, *27*, 457–459.
3. Ebbesen, T. W.; Lezec, H. J.; Ghaemi, H. F.; Thio, T.; Wolff, P. A. Extraordinary Optical Transmission through Sub-Wavelength Hole Arrays. *Nature* **1998**, *391*, 667–669.
4. Ghaemi, H. F.; Thio, T.; Grupp, D. E.; Ebbesen, T. W.; Lezec, H. J. Surface Plasmons Enhance Optical Transmission Through Subwavelength Holes. *Phys. Rev. B: Condens. Matter Mater. Phys.* **1998**, *58*, 6779–6782.
5. Barnes, W. L.; Dereux, A.; Ebbesen, T. W. Surface Plasmon Subwavelength Optics. *Nature* **2003**, *424*, 824–830.
6. Catrysse, P. B.; Wandell, B. A. Integrated Color Pixels in 0.18-μm Complementary Metal Oxide Semiconductor Technology. *J. Opt. Soc. Am. A* **2003**, *20*, 2293–2306.
7. Laux, E.; Genet, C.; Skauli, T.; Ebbesen, T. W. Plasmonic Photon Sorters for Spectral and Polarimetric Imaging. *Nat. Photonics* **2008**, *2*, 161–164.
8. Bravo-Abad, J.; Degiron, A.; Przybilla, F.; Genet, C.; García-Vidal, F. J.; Martín-Moreno, L.; Ebbesen, T. W. How Light Emerges From an Illuminated Array of Subwavelength Holes. *Nat. Phys.* **2006**, *2*, 120–123.
9. Chen, Q.; Das, D.; Chitnis, D.; Walls, K.; Drysdale, T. D.; Collins, S.; Cumming, D. R. S. A CMOS Image Sensor Integrated with Plasmonic Colour Filters. *Plasmonics* **2012**, *7*, 695–699.
10. Chen, Q.; Chitnis, D.; Walls, K.; Drysdale, T. D.; Collins, S.; Cumming, D. R. S. CMOS Photodetectors Integrated with Plasmonic Color Filters. *IEEE Photonics Technol. Lett.* **2012**, *24*, 197–199.
11. Chen, Q.; Cumming, D. R. S. High Transmission and Low Color Cross-Talk Plasmonic Color Filters Using Triangular-Lattice Hole Arrays in Aluminum Films. *Opt. Express* **2010**, *18*, 14056–14062.
12. Yokogawa, S.; Burgos, S. P.; Atwater, H. A. Plasmonic Color Filters for CMOS Image Sensor Applications. *Nano Lett.* **2012**, *12*, 4349–4354.
13. Lee, H.-S.; Yoon, Y.-T.; Lee, S.-S.; Kim, S.-H.; Lee, K.-D. Color Filter Based on a Subwavelength Patterned Metal Grating. *Opt. Express* **2007**, *15*, 15457–15463.
14. Pacifici, D.; Lezec, H. J.; Sweatlock, L. A.; Walters, R. J.; Atwater, H. A. Universal Optical Transmission Features in Periodic and Quasiperiodic Hole Arrays. *Opt. Express* **2008**, *16*, 9222–9238.
15. Ravets, S.; Rodier, J. C.; Ea Kim, B.; Hugonin, J. P.; Jacubowiez, L.; Lalanne, P. Surface Plasmons in the Young Slit Doublet Experiment. *J. Opt. Soc. Am. B* **2009**, *26*, B28–B33.
16. Gao, H.; Henzie, J.; Odom, T. W. Direct Evidence for Surface Plasmon-Mediated Enhanced Light Transmission Through Metallic Nanohole Arrays. *Nano Lett.* **2006**, *6*, 2104–2108.
17. Rotenberg, N.; Spasenović, M.; Krijger, T. L.; le Feber, B.; García de Abajo, F. J.; Kuipers, L. Plasmon Scattering From Single Subwavelength Holes. *Phys. Rev. Lett.* **2012**, *108*, 127402.
18. de León-Pérez, F.; García-Vidal, F. J.; Martín-Moreno, L. Role of Surface Plasmon Polaritons in the Optical Response of a Hole Pair. *Phys. Rev. B: Condens. Matter Mater. Phys.* **2011**, *84*, 125414.
19. Baudrion, A.-L.; de Léon-Pérez, F.; Mahboub, O.; Hohenau, A.; Ditlbacher, H.; García-Vidal, F. J.; Dintinger, J.; Ebbesen, T. W.; Martín-Moreno, L.; Krenn, J. R. Coupling Efficiency of Light to Surface Plasmon Polariton for Single Subwavelength Holes in a Gold Film. *Opt. Express* **2008**, *16*, 3420–3429.
20. Przybilla, F.; Degiron, A.; Genet, C.; Ebbesen, T. W.; de León-Pérez, F.; Bravo-Abad, J.; García-Vidal, F. J.; Martín-Moreno, L. Efficiency and Finite Size Effects in Enhanced Transmission Through Subwavelength Apertures. *Opt. Express* **2008**, *16*, 9571–9579.
21. Odom, T. W.; Gao, H.; McMahon, J. M.; Henzie, J.; Schatz, G. C. Plasmonic Superlattices: Hierarchical Subwavelength Hole Arrays. *Chem. Phys. Lett.* **2009**, *483*, 187–192.
22. Si, G.; Zhao, Y.; Liu, H.; Teo, S.; Zhang, M.; Jun Huang, T.; Danner, A. J.; Teng, J. Annular Aperture Array Based Color Filter. *App. Phys. Lett.* **2011**, *99*, 033105.
23. Sharma, G.; Wu, W.; Dalal, E. N. The CIEDE2000 Color-Difference Formula: Implementation Notes, Supplementary Test Data, and Mathematical Observations. *Color Res. Appl.* **2004**, *30*, 21–30.
24. Matsushima, K.; Sato, M.; Saito, S. *The Image Quality Standard based on Human Visual System for the Spectral Sensitivity Crosstalk Depending on Lens F-number*; Proceedings of the International Image Sensor Society, Snowbird, Utah USA, June 12−16, **2013**.
25. Barnes, W. L.; Murray, W. A.; Dintinger, J.; Devaux, E.; Ebbesen, T. W. Surface Plasmon Polaritons and Their Role in the Enhanced Transmission of Light Through Periodic Arrays of Subwavelength Holes in a Metal Film. *Phys. Rev. Lett.* **2004**, *92*, 107401.
26. Murray, W. A.; Astilean, S.; Barnes, W. L. Transition From Localized Surface Plasmon Resonance to Extended Surface Plasmon-Polariton as Metallic Nanoparticles Merge to Form a Periodic Hole Array. *Phys. Rev. B: Condens. Matter Mater. Phys.* **2004**, *69*, 165407.
27. Burgos, S. P.; de Waele, R.; Polman, A.; Atwater, H. A. A Single-Layer Wide-Angle Negative-Index Metamaterial at Visible Frequencies. *Nat. Mater.* **2010**, *9*, 407–412.
28. Salvi, J.; Roussey, M.; Baida, F. I.; Bernal, M.-P.; Mussot, A.; Sylvestre, T.; Maillotte, H.; Van Labeke, D.; Perentes, A.; Utke, I.; *et al.* Annular Aperture Arrays: Study in the Visible Region of the Electromagnetic Spectrum. *Opt. Lett.* **2005**, *30*, 1611–1613.
29. Marani, R.; D'Orazio, A.; Petruzzelli, V.; Rodrigo, S. G.; Martín-Moreno, L.; García-Vidal, F. J.; Bravo-Abad, J. Gain-Assisted Extraordinary Optical Transmission Through Periodic Arrays of Subwavelength Apertures. *New J. Phys.* **2012**, *14*, 013020.
30. Palik, E. D.; Ghosh, G. *Handbook of Optical Constants of Solids*; Academic Press: Orlando, FL, 1985.